Ising magnetoresistance induced by Ising spin-orbit coupling

Duo Zhao,[1] Jiaqian Sun,[2,3] Wei Tang,[1] and Yu-Jia Zeng[1,*]

[1]*Key Laboratory of Optoelectronic Devices and Systems of Ministry of Education and Guangdong Province, College of Physics and Optoelectronic Engineering, Shenzhen University, Shenzhen 518060, China*

[2]*Key Laboratory of Semiconductor Materials Science and Beijing Key Laboratory of Low Dimensional Semiconductor Materials and Devices, Institute of Semiconductors, Chinese Academy of Sciences, Beijing 100083, China*

[3]*Center of Materials Science and Optoelectronics Engineering, University of Chinese Academy of Sciences, Beijing 100190, China*

(Received 5 February 2023; revised 30 August 2023; accepted 31 August 2023; published 13 September 2023)

Ising (Zeeman-type) spin-orbit coupling (SOC) generated by in-plane inverse asymmetry has attracted considerable attention, especially in Ising superconductors and spin-valley coupling physics. However, many unconventional observations and emerging physical phenomena remain to be elucidated in low-symmetry two-dimensional materials. Here, we theoretically study the spin texture of σ_z (spin angular momentum projection along z) induced by Ising SOC in monolayer $1T_d$ WTe_2. We predict Ising magnetoresistance (MR), whose resistance depends on the out-of-plane magnetic moment in the monolayer WTe_2/ferromagnetic heterostructure. The Ising MR is believed to be an interesting counterpart to the well-studied spin Hall magnetoresistance. In addition, the unconventional charge-to-spin (named the Ising effect) and spin-to-charge conversion (named the inverse Ising effect) also contribute to the Ising MR. The recently observed "unconventional" spin-to-charge conversion can be well explained by the inverse Ising effect.

DOI: 10.1103/PhysRevB.108.094420

I. INTRODUCTION

Spin-orbit coupling (SOC) plays a key role in many emerging physical phenomena, such as Majorana zero-energy mode and Weyl nodes [1–6]. Also, spin Hall effect, spin-orbit torque, and many other magnetoresistances (MRs) are also induced by SOC [7–10]. In addition, Ising (Zeeman-type) SOC, which is generated by in-plane (IP) inversion asymmetry of two-dimensional (2D) materials [11,12], has attracted much attention, especially in Ising superconductors and spin-valley coupling on collective quantum phenomena [13–18]. In transition metal dichalcogenides (TMDs), particularly $1T_d$ WTe_2, detailed physical exploration on Ising SOC has been dramatically motivated by recent discoveries of nonlinear Hall effect, out-of-plane dampinglike torque, and unconventional spin-charge conversion [19–27].

Different types of MR induced by SOC are useful tools to explore the material's physical properties for spintronic applications [28]. Among them, spin Hall magnetoresistance (SMR) is an excellent platform to reveal the mechanisms of spin-orbit torque in heavy metal/ferromagnet bilayers [9,29–31]. Also, Rashba-Edelstein MR induced by Rashba SOC was observed in Bi/Ag/CoFeB and 2D/ferromagnet heterostructures [32–35]. SMR and Rashba-Edelstein MR have similar performances, which are therefore hardly distinguished experimentally. As for Ising SOC, the spin polarization direction, charge current, and spin current are not orthogonal to each other in the processes of spin-charge conversion. Therefore, the MR induced by Ising SOC is expected to provide a different platform to study spin and orbit related phenomena.

In this study, according to the symmetry analysis and first principles calculation, the distribution of σ_z in the band structure is well described. Based on this, we predict a type of MR, namely Ising MR, whose properties are different from that of SMR, i.e., when the magnetic moment ($\boldsymbol{M}$) of ferromagnet points to out of plane (OOP), the resistances are at the high and low states for SMR and Ising MR, respectively. In addition, the recently observed unconventional spin-to-charge conversion can be well explained by the named inverse Ising effect, which is the key physical mechanism of Ising MR.

II. RESULTS AND DISCUSSION

For monolayer $1T_d$ WTe_2, the double rotating symmetry C_{2a} is broken due to the slight distortion of W-Te bonding [Fig. 1(a)] [36,37]. The Hamiltonian of SOC can be written as $H_{SOC} \propto (\hat{\boldsymbol{\sigma}} \times \hat{\boldsymbol{p}}) \cdot (-\nabla V)$, where $\hat{\boldsymbol{\sigma}}$, $\hat{\boldsymbol{p}}$, and V represent the Pauli vector, momentum, and potential, respectively. In Cartesian coordinates, it can be written as

$$H_{SOC} = a(k_y\hat{\sigma}_x - k_x\hat{\sigma}_y) + \left(bk_x - \frac{c}{\hbar}k_y\right)\hat{\sigma}_z, \qquad (1)$$

where a, b, and c are the strength of SOC with the asymmetry direction along the $\boldsymbol{z}$, $\boldsymbol{y}$, and $\boldsymbol{x}$ axes, respectively; $\boldsymbol{k}$ is the wave vector.

From the crystal symmetry aspect, the symmetric operations acting on the H_{SOC} is located at $k_u\sigma_v$ (u and v represent x, y, and z). In the case of 2D materials, the k_z can be neglected.

*Corresponding author: yjzeng@szu.edu.cn

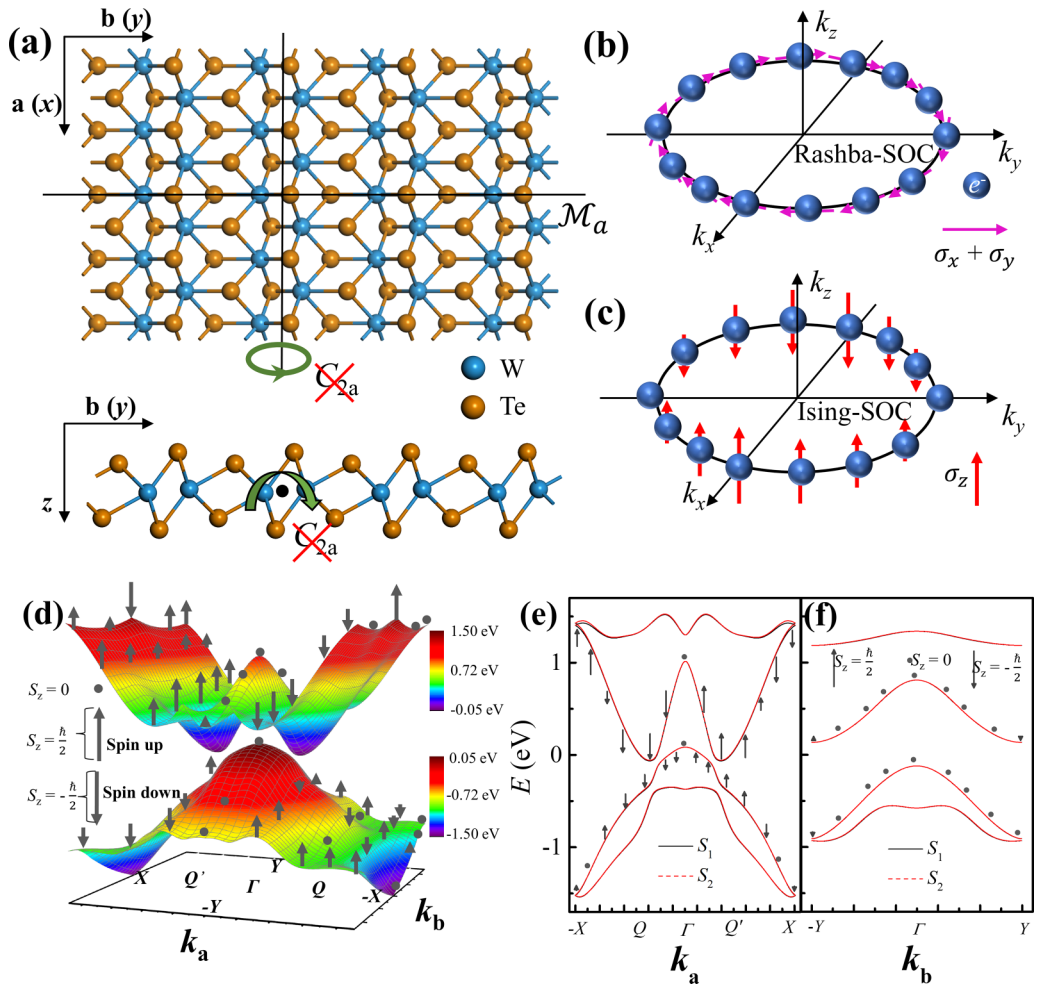

FIG. 1. (a) The top and side views of the crystal lattice $1T_d$ WTe_2. (b),(c) The spin texture of the Rashba SOC (b) and Ising SOC (c). (d) 3D band structure and spin texture of the $1T_d$ WTe_2 in the first Brillouin zone; the colors represent the energy values, and the arrow length and direction represent projected spin values (S_z) and spin directions. (e),(f) The band structure with σ_z distribution along $\boldsymbol{k}_a$ ($k_b = 0$) and $\boldsymbol{k}_b$ ($k_a = 0$) axes extracted from (d); the black line S_1 and red dashed line S_2 represent the spin splitting band structures due to SOC.

These operations acting on the $\boldsymbol{k}$ and $\vec{\sigma}$ can be expresed as

$$T(k_x, k_y, k_z)\,(-k_x, -k_y, -k_z) \quad \text{and} \quad T(\sigma_x, \sigma_y, \sigma_z)\,(-\sigma_x, -\sigma_y, -\sigma_z), \tag{2}$$

$$\mathcal{M}_a(k_x, k_y, k_z)\,(-k_x, k_y, k_z) \quad \text{and} \quad \mathcal{M}_a(\sigma_x, \sigma_y, \sigma_z)\,(\sigma_x, -\sigma_y, -\sigma_z), \tag{3}$$

$$C_{2a}(k_x, k_y, k_z)\,(k_x, -k_y, -k_z) \quad \text{and} \quad C_{2a}(\sigma_x, \sigma_y, \sigma_z)\,(\sigma_x, -\sigma_y, -\sigma_z). \tag{4}$$

All the $k_u\sigma_v$ operated by time-reversal symmetry (T) will keep invariant. With mirror symmetry ($\mathcal{M}_a$), the $k_x\sigma_y$, $k_x\sigma_z$, and $k_y\sigma_x$ are unchanged. For C_{2a} operation, $k_x\sigma_x$, $k_y\sigma_y$, and $k_y\sigma_z$ satisfy invariance. There are no common invariants about $k_u\sigma_v$, thus, no SOC would appear. However, when C_{2a} is broken, the $k_x\sigma_y$, $k_x\sigma_z$, and $k_y\sigma_x$ are the common invariants. Therefore, the H_{SOC} of the $1T_d$ WTe_2 can be written as

$$H_{\mathrm{SOC}} = \frac{a}{\hbar}(\hat{\boldsymbol{\sigma}} \times \hat{\boldsymbol{p}}) \cdot \hat{\boldsymbol{z}} + \frac{b}{\hbar}(\hat{\boldsymbol{\sigma}} \times \hat{\boldsymbol{p}}) \cdot \hat{\boldsymbol{y}} \tag{5}$$

To simplify our model and reflect the main physics, we use the effective Hamiltonian to describe the $1T_d$ WTe_2:

$$H = \left(\frac{\hat{p}^2}{2m}\right) + a(k_y\hat{\sigma}_x - k_x\hat{\sigma}_y) + \frac{b}{\hbar}k_x\hat{\sigma}_z. \tag{6}$$

After solving it, we obtain the expression of Rashba-SOC and Ising-SOC spin texture equations,

$$+|\sigma_x|+ = \frac{ak_y}{\sqrt{b^2k_x^2 + a^2\left(k_x^2 + k_y^2\right)}},\ -|\sigma_x|- = \frac{-ak_y}{\sqrt{b^2k_x^2 + a^2\left(k_x^2 + k_y^2\right)}}$$

$$\langle +|\sigma_y|+\rangle = \frac{-ak_x}{\sqrt{b^2k_x^2 + a^2\left(k_x^2 + k_y^2\right)}}, \langle -|\sigma_y|-\rangle = \frac{ak_x}{\sqrt{b^2k_x^2 + a^2\left(k_x^2 + k_y^2\right)}}, \tag{7}$$

$$\langle +|\sigma_z|+\rangle = \frac{bk_x}{\sqrt{b^2k_x^2 + a^2\left(k_x^2 + k_y^2\right)}}, \langle -|\sigma_z|-\rangle = \frac{-bk_x}{\sqrt{b^2k_x^2 + a^2\left(k_x^2 + k_y^2\right)}}, \tag{8}$$

which are intuitively displayed in Figs. 1(b) and 1(c), respectively.

To describe the distribution of σ_z in the Γ-centered first Brillouin zone and obtain the parameters, we performed density functional theory (DFT) calculations. In this work, all first-principles calculations were performed on JDFTX plane-wave DFT software [38]. The plane-wave basis was with the cutoff energy of 500 eV, and the generalized gradient approximation (GGA) [39] with Perdew-Burke-Ernzerhof (PBE) [40] exchange-correlation functional was used to estimate the band gap considering the SOC. Then, the Heyd-Scuseria-Ernzerhof (HSE) method [41] was used to adjust the band gap according to the previous works [36]. The monolayer $1T_d$ WTe_2 was constructed in vacuum with a thickness of approximately 16 Å. After performing the structure optimizations and self-consistent static state calculations, we performed with the k-point meshes of $160 \times 80 \times 1$ to obtain the band structure and spin texture. The convergent standard was 10^{-8} eV/atom. The three-dimensional (3D) band structure of $1T_d$ WTe_2 is shown in Fig. 1(d) accompanying with spin projected S_z. The length and direction of the grey arrows represent the splitting band's projecting values of S_z and spin directions, and the standard length of $|S_z|$ is $\frac{\hbar}{2}$. The color maps represent the energy values of the conduction band and valence band. Compared with the points $(-k_a, -k_b)$, the σ_z of the points (k_a, k_b) possess the opposite direction and the same $|S_z|$ value, which agree with the characteristic $H_{SOC} = \frac{b}{\hbar}\hat{p}_x\hat{\sigma}_z$. To directly display the σ_z distribution along the $\boldsymbol{k}_a$ ($k_b = 0$) and $\boldsymbol{k}_b$ ($k_a = 0$) axes, the band structures of these two axes are shown in Figs. 1(e) and 1(f), respectively. There is σ_z distribution along $\boldsymbol{k}_a$ ($k_b = 0$) axis, however, the distribution of σ_z along the $\boldsymbol{k}_b$ axis is almost $S_z = 0$. DFT results are consistent with Fig. 1(c).

To obtain the SOC strength, we used the $\boldsymbol{k}\cdot\boldsymbol{p}$ model to fit the band structure calculated by DFT. Previous works showed that the $\boldsymbol{k}\cdot\boldsymbol{p}$ model could capture the main physical pictures of the monolayer WTe_2 and well describe the band structures [36,42]. The $\boldsymbol{k}\cdot\boldsymbol{p}$ Hamiltonian for the monolayer $1T_d$ WTe_2 can be written as

$$H_{kp} = H_{kp}^0 + H_{SOC}, \tag{9}$$

where

$$H_{kp}^0 = A\left(k_x^2 + k_y^2\right)\tau_0 + \left[B\left(k_x^2 + k_y^2\right) + \delta\right]\tau_z + hk_y\tau_y \tag{10}$$

represents the spinless part of the Hamiltonian and τ_i ($i = x, y, z$) is the Pauli matrices in orbital space.

A and B are related to the effective masses of the valence and conduction bands, and δ describes the degree of the band inversion at the center of the first Brillouin zone. The h represents the crystalline anisotropy in the $\boldsymbol{x}$ direction. Here, we should consider the difference between Rashba-type SOC in the $\boldsymbol{x}$ and $\boldsymbol{y}$ directions. Therefore, the Hamiltonian of the SOC term for the monolayer $1T_d$ WTe_2 can be written as

$$H_{SOC} = \frac{a_1}{\hbar}\hat{p}_y\hat{\sigma}_x\tau_x + \frac{a_2}{\hbar}\hat{p}_x\hat{\sigma}_y\tau_x + \frac{b}{\hbar}\hat{p}_x\hat{\sigma}_z\tau_x. \tag{11}$$

The total seven parameters would determine the valence and conduction band structure of the monolayer $1T_d$ WTe_2. By fitting the DFT calculation result as shown in Figs. 2(b) and

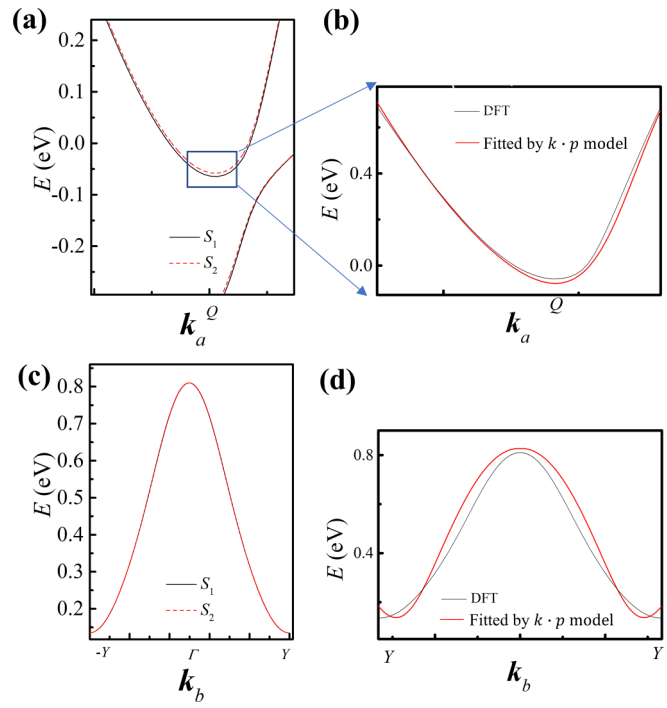

FIG. 2. (a) The zooming-in band structures calculated by DFT at around of $\boldsymbol{Q}$ point; S_1 and red dashed line S_2 represent the spin-splitting band structures due to SOC. (b) The fitted band structure calculated by DFT using the $\boldsymbol{k}\cdot\boldsymbol{p}$ model at $\boldsymbol{Q}$ point. (c),(d) The band structures calculated by DFT along $\boldsymbol{k}_b$ direction and the fitted band structure calculated by DFT using $\boldsymbol{k}\cdot\boldsymbol{p}$ model.

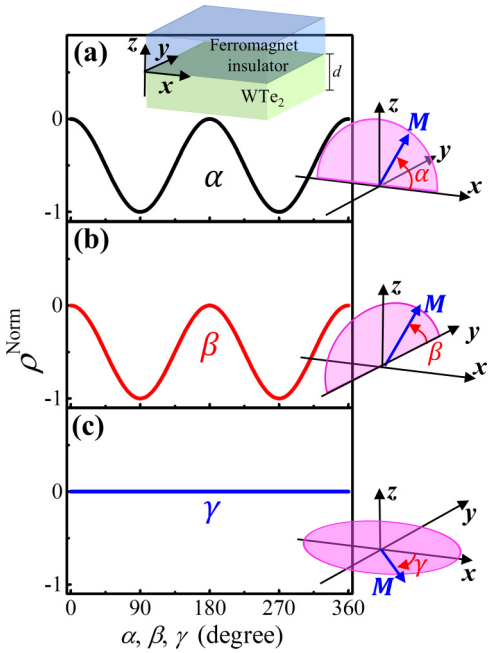

FIG. 3. (a)–(c) The performance of the normalized Ising MR ρ^{Norm} vs α, β, and γ with rotating $\boldsymbol{M}$ in three types of planes.

2(d), the SOC parameters a_1, a_2, and b are 0.072, 0.084, and -0.121 eV, respectively. The sign of b is obtained according to the spin textures. These values are close to that in Ref. [42].

Like the Rashba-Edelstein MR [43], we study the charge and spin transport in WTe_2/ferromagnetic insulator (FI) bilayers considering Ising SOC. As shown in Fig. 3(a) top panel, d is the thickness of monolayer WTe_2, occupying $z \in (-d, 0)$. The Hamiltonian of this system can be written as

$$H = \left(\frac{\hat{\boldsymbol{p}}^2}{2m}\right) + H_M + H_V + \frac{b}{\hbar}(\hat{\boldsymbol{\sigma}} \times \hat{\boldsymbol{p}}) \cdot \hat{\boldsymbol{y}}, \tag{12}$$

where $H_M = J\boldsymbol{\sigma} \cdot \boldsymbol{M}\Pi(z)$ and $H_V = V_+\Pi(-z-d) + V\Pi(z)$ are the exchange interaction of the FI and confining potential of the monolayer $1T_d$ WTe_2 at the vacuum and FI interfaces. Π is the Heaviside unit step function. We treated $V_+ \to +\infty$, and the electrons in WTe_2 can penetrate to the FI layer depth $t = \sqrt{\frac{\hbar^2}{2mV}}$. Therefore, the effective thickness of the free electrons is $d' = d + t$. The exchange interaction would induce the penetration depth t spin-dependent $t_s = t(1 - \frac{sJ}{2V})$, where $s = \pm 1$ represents spin, and the spin-dependent effective thickness of the free electrons is $d_s = d + t_s$. We treated H_{SOC} as the perturbation term to $H_0 = (\frac{\hat{p}^2}{2m}) + H_M + H_V$. The eigenenergy and eigenstates of the H_0 are

$$E_0^{ns} = E_{nq} + sE_nE_j,$$
$$\psi_0^{ns} = \frac{e^{i\vec{r}\cdot\vec{k}}}{\sqrt{2d_s}}\sin[k_{ns}(z + t_s)]|s\rangle_{\vec{M}}, \tag{13}$$

where $k_{ns} = \frac{n\pi}{d_s}$, $k_n = \frac{n\pi}{d'} = \frac{n\pi}{d}$, and $\boldsymbol{k}$ are the quantized wave vector due to the confined potential of H_V and in-plane wave vectors. $E_n = \frac{\hbar^2 k_n^2}{2m}$ and $E_{nq} = \frac{\hbar^2 \boldsymbol{k}^2}{2m} + E_n$. We select $\boldsymbol{M}$ as the spin quantum projection axis, and $|s\rangle_{\vec{M}}$ is the spinor solving $\vec{\boldsymbol{\sigma}} \cdot \vec{\boldsymbol{M}}|s\rangle_{\vec{M}} = s|s\rangle_{\vec{M}}$. According to the perturbation theory, we obtain the eigenenergy and eigenstates to the first correction:

$$E^{ns} = E_0^{ns} - sbk_F\boldsymbol{M} \cdot \frac{\boldsymbol{y} \times \boldsymbol{k}}{k_F},$$
$$\psi^{ns} = \psi_0^{ns} - \frac{sbk_F}{2E_nE_j}\hat{\boldsymbol{\sigma}}_{s's} \cdot \frac{\boldsymbol{y} \times \boldsymbol{k}}{k_F}\psi_0^{ns'}, \tag{14}$$

where $\hat{\boldsymbol{\sigma}}_{s's} = \langle s'|\vec{\boldsymbol{\sigma}}|s\rangle_{\vec{M}}$ and $s' = -s$. We can calculate the charge current in the presence of electric field in the x direction ($\boldsymbol{E}_x$). According to the velocity operator $\hat{\boldsymbol{v}} = -\frac{i}{\hbar}[\hat{\boldsymbol{r}}, H]$, the average value of electrons velocity $\boldsymbol{v}(\boldsymbol{k}) = \langle\psi^{ns}|\hat{\boldsymbol{v}}|\psi^{ns}\rangle$ and the electric field-induced drift reflected by the distribution function $g(k) = \frac{e\tau}{\hbar}\delta(E^{ns} - E_F)\frac{\partial E^{ns}}{\partial \boldsymbol{q}} \cdot \boldsymbol{E}_{\boldsymbol{x}}$, we calculate the charge current density $\boldsymbol{J} = e\Sigma_{ns}\int d^2\boldsymbol{k}g(\boldsymbol{k})\boldsymbol{v}(\boldsymbol{k})$. The longitudinal conductance can be written as

$$\sigma_{xx} = d\sigma_0 + \sigma_0\frac{3b^2}{20}\left(2 + M_z^2\right), \tag{15}$$

where $\sigma_0 = \frac{e^2k_F^3\tau}{3\pi^2m}$ is the Drude conductance. Here, we name the MR induced by the Ising SOC the Ising MR. According to the $b = -0.121$ eV, the ratio of the Ising MR $r = \frac{\rho^\perp - \rho^\parallel}{\rho^\perp} = 0.2\%$ is comparable with that of SMR [44], where $\rho^\perp$ and $\rho^\parallel$ represent the resistivities when $\boldsymbol{M}$ is parallel and perpendicular to the $\boldsymbol{z}$. The changes of $\rho^{\text{Norm}} = \frac{\rho_{xx} - \rho^\perp}{\rho^\perp - \rho^\parallel}$ at three different planes are shown in Fig. 3. According to Eq. (15), ρ^{Norm} can be written as

$$\rho^{\text{Norm}} = \tfrac{1}{2}[\cos(2\theta) - 1], \tag{16}$$

where θ is the angle of the $\boldsymbol{M}$ with the sample plane. For Figs. 3(a) and 3(b), θ is α and β. As for Fig. 3(c), the θ keeps 0 with the change of γ. The ρ^{Norm} thus remains 0.

In reality, the Ising SOC and Rashba SOC coexist inevitably, which influences the performance of R^{Norm}. We define the spin-orbit angle ϑ in Fig. 4, and the strengths of Ising SOC and Rashba SOC can be written as $a = \gamma\cos\vartheta$ and $b = \gamma\sin\vartheta$, respectively [45]. The values of the ϑ represent the relative strength of Ising SOC and Rashba SOC. As $\vartheta = 0°$, it means only Ising SOC exists. And $\vartheta = 90°$, only Rashba SOC exists. The function of ρ^{Norm} can be refined as

$$\rho^{\text{Norm}} = \tfrac{1}{2}[\cos(2\beta + 2\vartheta) - 1]. \tag{17}$$

To display the change process of the MR with ϑ, we also plot $\rho^{\text{Norm}} - \beta$ curves of several ϑ values, which are displayed in Fig. 4 according to Eq. (17). The ϑ value of the monolayer WTe_2 calculated by DFT is approximately 57°. However, the angle values may vary due to the presence of Rashba SOC and other complicated SOC [46,47]. In practice, the value of the ϑ can be easily obtained from the $\rho^{\text{Norm}} - \beta$ curve experimentally. Therefore, the relative strength of Ising SOC and Rashba SOC can be separated according to the ϑ. In addition, to simplify our calculation, we assume that the ferromagnetic layer is an insulator. Nevertheless, the presence of metallic ferromagnetic material would not influence the Ising MR when the $\boldsymbol{M}$ is rotated in the $\boldsymbol{y}$ - $\boldsymbol{z}$ plane.

When the $\boldsymbol{M}$ is rotated in the $\boldsymbol{x}$ - $\boldsymbol{z}$ plane, the change of the ρ^{Norm} with α is shown in Fig. 5(b) as long as $\vartheta \neq 90°$. That is because the M is always orthogonal to the Rashba-SOC component along $\boldsymbol{y}$, as shown in Fig. 5(a). Then, the

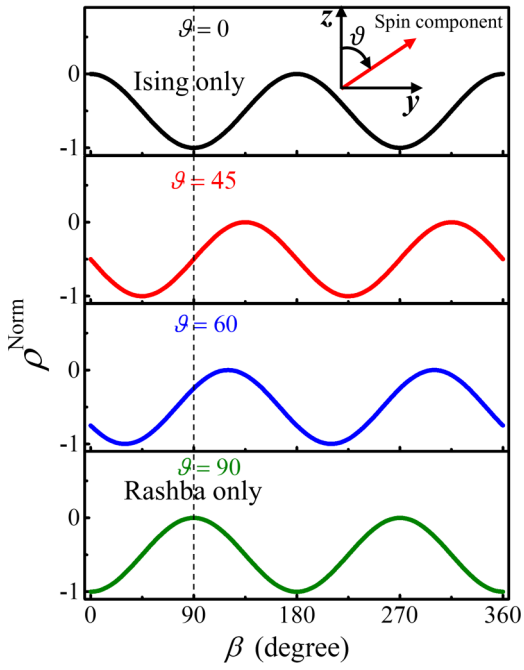

FIG. 4. The evolution of the ρ^{Norm}-β with spin-orbit angle ϑ considering Ising SOC and Rashba SOC in $1T_{\mathrm{d}}$ WTe_2/FM heterostructure.

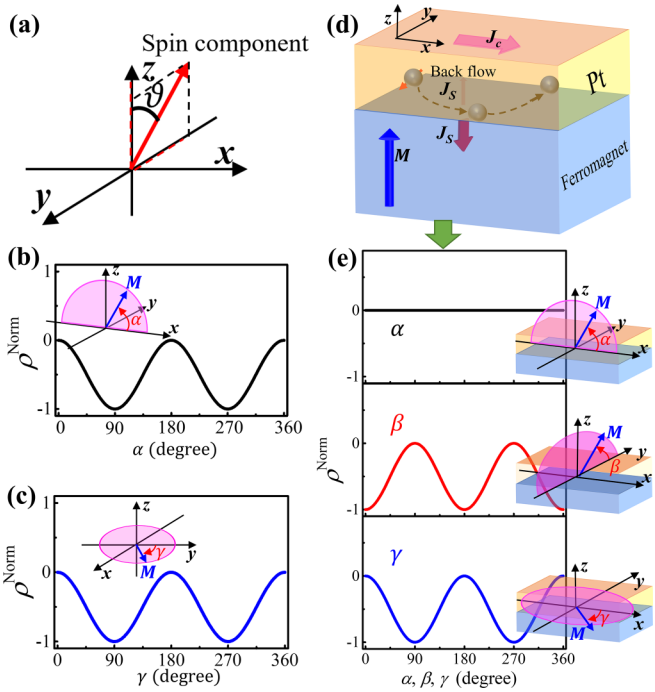

FIG. 5. (a) The spin component with external current applied along $\boldsymbol{x}$. (b),(c) The evolution of the normalized MR with spin-orbit angle ϑ when the $\boldsymbol{M}$ rotation in the $\boldsymbol{x}$-$\boldsymbol{z}$ and $\boldsymbol{y}$-$\boldsymbol{z}$ planes. (d) The schematic images of the geometric relation between the flow of electrons and spin accumulation in Pt/FM heterostructure. (e) The performance normalized SMR ρ^{Norm} vs α, β, and γ with rotating $\boldsymbol{M}$ of the ferromagnetic layer in three types of planes shown on the right side.

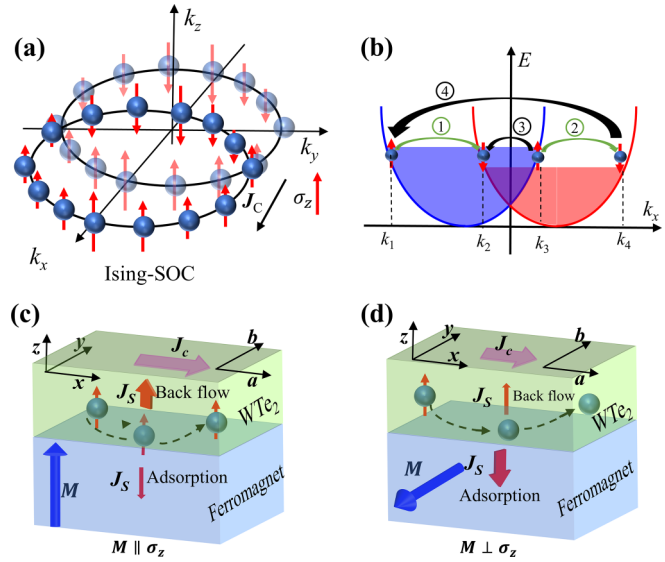

FIG. 6. (a) The spin texture of Ising SOC induced by the current along the $\boldsymbol{x}$-axis direction. (b) A one-dimensional band structure sketch of the spin-galvanic current induced by Ising SOC. (c),(d) The schematic images of the geometric relation between the flow of electrons and spin accumulation in $1T_{\mathrm{d}}$ WTe_2/FM heterostructure.

Rashba-Edelstein MR would always stay at zero, and there would be Ising MR only. When the $\boldsymbol{M}$ is rotated in the $\boldsymbol{x}$ - $\boldsymbol{y}$ plane, the change of the ρ^{Norm} with γ is shown in Fig. 5(c), as long as $\vartheta \neq 0^{\circ}$. At this condition, the M is always orthogonal to the Ising-SOC component along z as shown in Fig. 5(a). Then, the Ising MR would stay at zero, and there would be the Rashba-Edelstein MR only. The shape of the normalized MR would have no relation with ϑ when the $\boldsymbol{M}$ is rotated in the $\boldsymbol{x}$ - $\boldsymbol{z}$ and $\boldsymbol{x}$ - $\boldsymbol{y}$ planes. However, the resistance oscillate amplitude $\Delta\rho$ would be $\Delta\rho_\alpha = \Delta\rho_\beta \cos\vartheta$ and $\Delta\rho_\gamma = \Delta\rho_\beta \sin\vartheta$ according to the definition of the spin-orbit angle, where $\Delta\rho_\alpha$, $\Delta\rho_\beta$, and $\Delta\rho_\gamma$ are the resistivity oscillating amplitudes when the $\boldsymbol{M}$ is rotated in the $\boldsymbol{x}$ - $\boldsymbol{z}$, $\boldsymbol{y}$ - $\boldsymbol{z}$, and $\boldsymbol{x}$ - $\boldsymbol{y}$ planes, respectively.

The Ising MR can also be understood from another point of view, i.e., the inverse spin-galvanic effect and spin-galvanic effect, which are both induced by Ising SOC. To simplify the description here, we name them the Ising effect and inverse Ising effect, respectively. The spin direction in $1T_d$ WTe_2 with $\pm k_{\mathrm{a}}$ wave vector would point to $\pm z$. When the external current is applied to the $\boldsymbol{a}$ axis, the symmetric distribution of the wave vector is broken [Fig. 6(a)]. As a result, the spin polarization along z would be generated, i.e., the Ising effect, and the spin polarization is proportional to the external current. This is believed to be the origin of the nonlinear Hall effect and out-of-plane dampinglike torque found by a series of works recently [19,20].

As for the inverse Ising effect, it can be described by the phenomenological equation

$$j_x = Q_{xz} S_z. \tag{18}$$

The spin accumulation S_z and second-rank pseudotensor components Q_{xz} both determine the inverse Ising effect. The microscopic mechanism of the inverse Ising effect is due to asymmetric spin-flip relaxation of the nonequilibrium

spin-polarized electrons. In terms of energy conversion, this phenomenon is the transformation of nonequilibrium spin chemical potential into charge potential. The scattering matrix element of the spin-flip processes $|\uparrow, k_i\rangle \rightarrow |\downarrow, k_j\rangle$ are related to $[v(k_j - k_i)]^2(k_i + k_j)^2$. Processes 1 and 2 in Fig. 6(b), marked with green arrows, have the same spin scattering possibility due to $k_2 - k_1 = k_4 - k_3$ and $(k_2 + k_1)^2 = (k_4 + k_3)^2$. Therefore, they preserve the symmetric distribution of electrons, and no current appears. As for processes 3 and 4 depicted by black arrows [Fig. 6(b)], if the elastic scattering arises, i.e., $|k_1| = |k_4|$ and $|k_2| = |k_3|$, $(k_2 + k_1)^2 = 0$ and the possibility of the spin scattering vanishes. Therefore, the appearance of charge current requires inelastic scattering. On account of spin polarization, in reality, the spin scattering from spin up to spin down is inelastic, because the initial and final states are not at the same energy level.

The spin accumulation in WTe_2 can induce the inverse Ising effect. The spin accumulation (the value of S_z) and Q_{xz} both determine the inverse Ising effect. Similar to the inverse Rashba-Edelstein effect, the physical mechanism is mainly based on the property of spin-momentum locking. Only considering the Ising SOC, $H_{SOC} = -bk_x\sigma_z$. Electron's wave vector k_x is locked with σ_z. b can represent the strength of the symmetry breaking and the strength of the spin-momentum locking. Then, b should be proportional to Q_{xz}. According to the description of Fig. 6(b), the spin-dependent part of the electron scattering matrix $\boldsymbol{M}_{k_i,\,k_j}$ can be written as [48]

$$\boldsymbol{M}_{k_i,\,k_j} = A_{k_i,\,k_j}\boldsymbol{I} + \boldsymbol{\sigma}\cdot\boldsymbol{B}_{k_i,\,k_j}, \tag{19}$$

where $A_{k_i,\,k_j}$ and $\boldsymbol{I}$ is the spin scattering independent of SOC and unit matrix. $\boldsymbol{\sigma}\cdot\boldsymbol{B}_{k_i,\,k_j}$ can be written as

$$\boldsymbol{\sigma}\cdot\boldsymbol{B}_{k_i,\,k_j} = v(k_j - k_i)\sigma_z k_x. \tag{20}$$

Equation (20) determines the spin relaxation time τ_s. Therefore, the charge current, for instance in the $\boldsymbol{y}$ direction, can be written as

$$j_x = Q_{xz}S_z \propto en_e\frac{b}{\hbar}\frac{\tau_p\tau_s}{\tau_s'}S_z, \tag{21}$$

where τ_s' is the Elliot-Yafet spin-relaxation time, which is proportional to the momentum-relaxation time τ_p, and τ_s is the total spin-relaxation time.

In WTe_2/FM heterostructure [Fig. 6(c)], an external current $\boldsymbol{J}_C$ will generate spin accumulation at the interface of heterostructure. Then, the spin current $\boldsymbol{J}_S$ towards the FM layer would occur. When $\boldsymbol{M}$ points to OOP, the $\boldsymbol{J}_S$ with σ_z is rarely absorbed by the FM layer, and the back flowed $\boldsymbol{J}_S$ will generate the voltage due to the inverse Ising effect. At this condition, the measured resistance (R_{xx}) is small. When the $\boldsymbol{M}$ of the FM layer points to IP in Fig. 6(d), the spin current with OOP spin polarization is absorbed by the FM layer and drives the procession of $\boldsymbol{M}$. Then, the R_{xx} of WTe_2 would stay unchanged.

In addition, the inverse Ising effect in $1T_d$ WTe_2 would cause "unconventional" spin-to-charge conversion. To describe these unconventional phenomena concretely, we introduce a spin-to-charge model as shown in Fig. 7(a). A charge current is applied to a ferromagnetic electrode ($F1$) and flows out from electrode $F2$. We choose graphene as the spin-transmission channel owing to its long spin diffusion

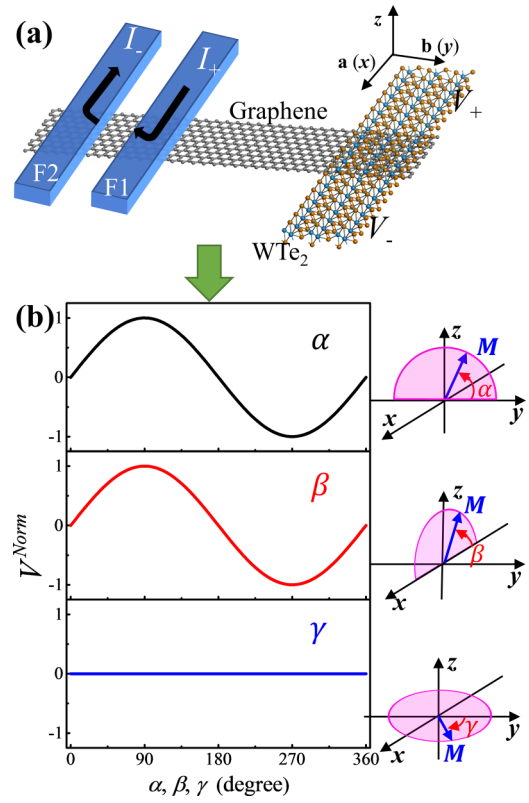

FIG. 7. (a) Sketch structure of the inverse Ising effect induced by $1T_d$$WTe_2$. (b) The change of the normalized voltage (V^{Norm}) generated by inverse Ising effect with α, β, and γ under rotation of the $\boldsymbol{M}$.

length [21,49]. The spin current from $F1$ would pour into the graphene channel. Driven by the spin chemical potential, the spin current would flow toward the $1T_d$ WTe_2 side. Only considering the action of the inverse Ising effect, the WTe_2 layer would absorb the spin current with σ_z and produce the voltage. Rotating $\boldsymbol{M}$ of the $F1$ will change the spin polarized direction, then the voltage values generated by the inverse Ising effect can be described by

$$V \propto j_x = Q_{xz}S_z \propto en_e\frac{b}{\hbar}\frac{\tau_p\tau_s}{\tau_s'}S_z = en_e\frac{b}{\hbar}\frac{\tau_p\tau_s}{\tau_s'}\sin\theta. \tag{22}$$

When the $\boldsymbol{M}$ of $F1$ is rotated in the $\boldsymbol{y}$ - $\boldsymbol{z}$ and $\boldsymbol{x}$ - $\boldsymbol{z}$ planes, the θ equals α and β, and the change of the normalized $V^{Norm} = \frac{V}{V_\perp}$ with α and β are shown in Fig. 7(b), where $V_\perp$ is the voltage when $\theta = \frac{\pi}{2}$. When the $\boldsymbol{M}$ of $F1$ is rotated in the $\boldsymbol{x}$ - $\boldsymbol{y}$ plane, the θ is always 0. Thus, the V^{Norm} remains 0 regardless of the angle γ (the angle between $\boldsymbol{y}$ and $\boldsymbol{M}$) [Fig. 7(b)].

Considering the coexistence of Rashba-SOC and Ising SOC, Eq. (22) can be written as $V \propto en_e\frac{b}{\hbar}\frac{\tau_p\tau_s}{\tau_s'}\sin(\theta + \vartheta)$. Within the scope of SOC, Rashba SOC and bulk SOC have similar performances, and their spin-to-charge conversions cannot be distinguished experimentally. As shown in Fig. 8(a), WTe_2 is the spin sink layer to detect the voltage along the $\boldsymbol{a}$ ($\boldsymbol{x}$) direction. Here, we mainly discuss the evolution of the normalized voltage (V^{Norm}) with ϑ in the $\boldsymbol{y}$ - $\boldsymbol{z}$ plane. For

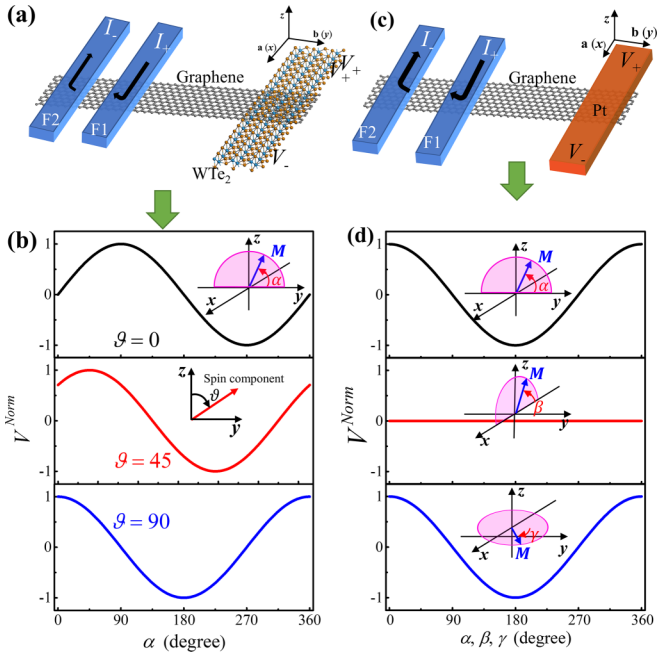

FIG. 8. (a) Sketch structure to confirm the inverse Ising effect induced by $1T_d WTe_2$. (b) The evolution of the V^{Norm} generated by the inverse Ising effect and inverse Rashba-Edelstein effect with spin-orbit angle ϑ in $1T_d WTe_2$ under rotating $\boldsymbol{M}$ of the ferromagnetic electrode ($F1$) in the $\boldsymbol{y}$-$\boldsymbol{z}$ plane. (c) The schematic model to character inverse spin Hall effect induced by Pt. (d) The V^{Norm} vs α, β, and γ curves in three different planes generated by inverse spin Hall effect in (c).

$\vartheta = 0$, the V^{Norm} vs ϑ is the pure inverse Ising effect curve as shown in the top panel of Fig. 8(b). Assuming that the strength of the Rashba SOC is the same as Ising SOC, the direction of the spin component in the $\boldsymbol{y}$ - $\boldsymbol{z}$ plane is $\vartheta = 45^\circ$. When the direction of the spin polarization is parallel ($\alpha = 45^\circ$) to and antiparallel ($\alpha = 225^\circ$) to the spin component, the values of V^{Norm} approach the maximum and minimum, respectively. As the direction of M of the $F1$ is orthogonal to the spin component, i.e., $\alpha = 135^\circ$ and 315°, the projection of spin to the spin component is zero, then the V^{Norm} is also zero. In short, whatever the value of ϑ, when the spin component is collinear with the $\boldsymbol{M}$, $|V^{\text{Norm}}|$ is equal to 1, and when the $\boldsymbol{M}$ is orthogonal to the spin component, V^{Norm} is zero, as shown in the bottom panel of Fig. 8(b). The voltage induced by inverse spin Hall effect such as that in Pt/ferromagnetic bilayers along the $\boldsymbol{a}$ direction is mainly contributed by the σ_y component of spin current rather than the σ_z, and it is proportional to S_y as shown in Figs. 8(c) and 8(d).

It is worth mentioning that recently reported "anisotropic magnetoresistance" (AMR) in monolayer WTe_2 [28,50–52] has essential physical differences with the proposed Ising MR in monolayer WTe_2/FI bilayers. The appearance of the AMR in monolayer WTe_2 is caused by a special topological band structure (gapless edge states). However, the Ising MR would appear only considering the Ising SOC and exchange interaction in Eq. (12). This is also the reason why we use the free electron model to derive the Ising MR, which can not only simplify our derivation but also avoid confusion with AMR. The Ising MR can appear at room temperature because Ising SOC persists at room temperature, however, the AMR in monolayer WTe_2 disappears at 100 K.

III. CONCLUSION

We have demonstrated the generation of σ_z considering Ising SOC in $1T_d WTe_2$, and predict an interesting phenomenon, namely Ising MR, which originates from the combination of the Ising effect and inverse Ising effect, in which the σ_z does not obey the rule of $\boldsymbol{j}_c \propto \boldsymbol{j}_s \times \boldsymbol{\sigma}$. Ising MR is believed to be a promising complement to the well-known SMR and Rashba-Edelstein MR. We also explain the recently observed unconventional spin-to-charge conversion by the inverse Ising effect. Our work broadens the understanding of emerging SOC and related physical phenomena, which provides opportunities to the fields of spintronics and multiferroics.

ACKNOWLEDGMENTS

This work was supported by the National Natural Science Foundation of China (Grant No. 52273298), the Guangdong Basic and Applied Basic Research Foundation (Grant No. 2022A1515010649), and the Shenzhen Science and Technology Program (Grants No. JCYJ20210324095611032, No. JCYJ20220818100204010, and No. JCYJ20220818100008016).

[1] C. L. Kane and E. J. Mele, Phys. Rev. Lett. **95**, 226801 (2005).
[2] A. Manchon, H. C. Koo, J. Nitta, S. M. Frolov, and R. A. Duine, Nat. Mater. **14**, 871 (2015).
[3] A. A. Burkov and L. Balents, Phys. Rev. Lett. **107**, 127205 (2011).
[4] L. Fu and C. L. Kane, Phys. Rev. Lett. **100**, 096407 (2008).
[5] D. Xiao, M. C. Chang, and Q. Niu, Rev. Mod. Phys. **82**, 1959 (2010).
[6] L. Sheng, D. N. Sheng, C. S. Ting, and F. D. M. Haldane, Phys. Rev. Lett. **95**, 136602 (2005).
[7] J. Sinova, D. Culcer, Q. Niu, N. A. Sinitsyn, T. Jungwirth, and A. H. MacDonald, Phys. Rev. Lett. **92**, 126603 (2004).
[8] A. Manchon and S. Zhang, Phys. Rev. B **78**, 212405 (2008).
[9] Y. T. Chen, S. Takahashi, H. Nakayama, M. Althammer, S. T. B. Goennenwein, E. Saitoh, and G. E. W. Bauer, Phys. Rev. B **87**, 144411 (2013).
[10] W. Tang, H. L. Liu, Z. Li, A. L. Pan, and Y. J. Zeng, Adv. Sci. **8**, 2100847 (2021).
[11] L. K. Shi and J. C. W. Song, Phys. Rev. B **99**, 035403 (2019).
[12] B. J. Feng, Y. H. Chan, Y. Feng, R. Y. Liu, M. Y. Chou, K. Kuroda, K. Yaji, A. Harasawa, P. Moras, A. Barinov, W. Malaeb, C. Bareille, T. Kondo, S. Shin, F. Komori, T. C. Chiang, Y. G. Shi, and I. Matsuda, Phys. Rev. B **94**, 195134 (2016).

[13] X. X. Xi, Z. F. Wang, W. W. Zhao, J. H. Park, K. T. Law, H. Berger, L. Forro, J. Shan, and K. F. Mak, Nat. Phys. **12**, 139 (2016).

[14] B. T. Zhou, N. F. Q. Yuan, H. L. Jiang, and K. T. Law, Phys. Rev. B **93**, 180501(R) (2016).

[15] S. C. de la Barrera, M. R. Sinko, D. P. Gopalan, N. Sivadas, K. L. Seyler, K. Watanabe, T. Taniguchi, A. W. Tsen, X. D. Xu, D. Xiao, and B. M. Hunt, Nat. Commun. **9**, 1427 (2018).

[16] K. F. Mak, K. L. McGill, J. Park, and P. L. McEuen, Science **344**, 1489 (2014).

[17] H. L. Zeng, J. F. Dai, W. Yao, D. Xiao, and X. D. Cui, Nat. Nanotechnol. **7**, 490 (2012).

[18] S. Ok, L. Muechler, D. Di Sante, G. Sangiovanni, R. Thomale, and T. Neupert, Phys. Rev. B **99**, 121105(R) (2019).

[19] D. MacNeill, G. M. Stiehl, M. H. D. Guimaraes, R. A. Buhrman, J. Park, and D. C. Ralph, Nat. Phys. **13**, 300 (2017).

[20] I. H. Kao, R. Muzzio, H. T. Zhang, M. L. Zhu, J. Gobbo, S. Yuan, D. Weber, R. Rao, J. H. Li, J. H. Edgar, J. E. Goldberger, J. Q. Yan, D. G. Mandrus, J. Hwang, R. Cheng, J. Katoch, and S. Singh, Nat. Mater. **21**, 1029 (2022).

[21] B. Zhao, B. Karpiak, D. Khokhriakov, A. Johansson, A. M. Hoque, X. G. Xu, Y. Jiang, I. Mertig, and S. P. Dash, Adv. Mater. **32**, 2000818 (2020).

[22] P. Song, C. H. Hsu, G. Vignale, M. Zhao, J. W. Liu, Y. J. Deng, W. Fu, Y. P. Liu, Y. B. Zhang, H. Lin, V. M. Pereira, and K. P. Loh, Nat. Mater. **19**, 292 (2020).

[23] F. Xue, C. Rohmann, J. W. Li, V. Amin, and P. Haney, Phys. Rev. B **102**, 014401 (2020).

[24] L. F. Zhang, J. Jiang, C. Multunas, C. Ming, Z. Z. Chen, Y. Hu, Z. H. Lu, S. Pendse, R. Jia, M. Chandra, Y. Y. Sun, T. M. Lu, Y. Ping, R. Sundararaman, and J. Shi, Nat. Photon. **16**, 529 (2022).

[25] C. K. Safeer, N. Ontoso, J. Ingla-Aynes, F. Herling, V. T. Pham, A. Kurzmann, K. Ensslin, A. Chuvilin, I. Robredo, M. G. Vergniory *et al.*, Nano Lett. **19**, 8758 (2019).

[26] Q. Ma, S. Y. Xu, H. T. Shen, D. MacNeill, V. Fatemi, T. R. Chang, A. M. M. Valdivia, S. F. Wu, Z. Z. Du, C. H. Hsu *et al.*, Nature (London) **565**, 337 (2019).

[27] K. F. Kang, T. X. Li, E. Sohn, J. Shan, and K. F. Mak, Nat. Mater. **18**, 324 (2019).

[28] P. Li, W. K. Wu, Y. Wen, C. H. Zhang, J. W. Zhang, S. F. Zhang, Z. M. Yu, S. Y. A. Yang, A. Manchon, and X. X. Zhang, Nat. Commun. **9**, 3990 (2018).

[29] M. Weiler, M. Althammer, F. D. Czeschka, H. Huebl, M. S. Wagner, M. Opel, I. M. Imort, G. Reiss, A. Thomas, R. Gross *et al.*, Phys. Rev. Lett. **108**, 106602 (2012).

[30] Y. T. Chen, S. Takahashi, H. Nakayama, M. Althammer, S. T. B. Goennenwein, E. Saitoh, and G. E. W. Bauer, J. Phys.: Condens. Matter **28**, 103004 (2016).

[31] T. Lin, C. Tang, H. M. Alyahayaei, and J. Shi, Phys. Rev. Lett. **113**, 037203 (2014).

[32] H. Nakayama, Y. Kanno, H. Y. An, T. Tashiro, S. Haku, A. Nomura, and K. Ando, Phys. Rev. Lett. **117**, 116602 (2016).

[33] S. L. Ding, Z. Y. Liang, D. Go, C. Yun, M. Z. Xue, Z. Liu, S. Becker, W. N. Yang, H. L. Du, C. S. Wang *et al.*, Phys. Rev. Lett. **128**, 067201 (2022).

[34] J. B. S. Mendes, S. M. Rezende, and J. Holanda, Phys. Rev. B **104**, 014408 (2021).

[35] X. Z. Chen, H. Bai, Y. C. Ji, Y. J. Zhou, L. Y. Liao, Y. F. You, W. X. Zhu, Q. Wang, L. Han, X. Y. Liu *et al.*, Nat. Electron. **5**, 574 (2022).

[36] S. Y. Xu, Q. Ma, H. T. Shen, V. Fatemi, S. F. Wu, T. R. Chang, G. Q. Chang, A. M. M. Valdivia, C. K. Chan, Q. D. Gibson *et al.*, Nat. Phys. **14**, 900 (2018).

[37] S. F. Wu, V. Fatemi, Q. D. Gibson, K. Watanabe, T. Taniguchi, R. J. Cava, and P. Jarillo-Herrero, Science **359**, 76 (2018).

[38] R. Sundararaman, K. Letchworth-Weaver, K. A. Schwarz, D. Gunceler, Y. Ozhabes, and T. A. Arias, SoftwareX **6**, 278 (2017).

[39] J. P. Perdew, K. Burke, and M. Ernzerhof, Phys. Rev. Lett. **77**, 3865 (1996).

[40] J. P. Perdew, K. Burke, and M. Ernzerhof, Phys. Rev. Lett. **78**, 1396 (1997).

[41] J. Heyd, G. E. Scuseria, and M. Ernzerhof, J. Chem. Phys. **118**, 8207 (2003).

[42] J. H. Garcia, M. Vila, C. H. Hsu, X. Waintal, V. M. Pereira, and S. Roche, Phys. Rev. Lett. **125**, 256603 (2020).

[43] V. L. Grigoryan, W. Guo, G. E. W. Bauer, and J. Xiao, Phys. Rev. B **90**, 161412(R) (2014).

[44] H. Nakayama, M. Althammer, Y. T. Chen, K. Uchida, Y. Kajiwara, D. Kikuchi, T. Ohtani, S. Geprags, M. Opel, S. Takahashi *et al.*, Phys. Rev. Lett. **110**, 206601 (2013).

[45] F. S. Bergeret and I. V. Tokatly, Phys. Rev. B **89**, 134517 (2014).

[46] M. Gmitra and J. Fabian, Phys. Rev. B **92**, 155403 (2015).

[47] M. Gmitra, D. Kochan, P. Hogl, and J. Fabian, Phys. Rev. B **93**, 155104 (2016).

[48] S. D. Ganichev, P. Schneider, V. V. Bel'kov, E. L. Ivchenko, S. A. Tarasenko, W. Wegscheider, D. Weiss, D. Schuh, B. N. Murdin, P. J. Phillips *et al.*, Phys. Rev. B **68**, 081302(R) (2003).

[49] W. Yan, L. C. Phillips, M. Barbone, S. J. Hamalainen, A. Lombardo, M. Ghidini, X. Moya, F. Maccherozzi, S. van Dijken, S. S. Dhesi *et al.*, Phys. Rev. Lett. **117**, 147201 (2016).

[50] C. Tan, M. X. Deng, G. L. Zheng, F. X. Xiang, S. Albarakati, M. Algarni, L. Farrar, S. Alzahrani, J. Partridge, J. B. Yi *et al.*, Nano Lett. **21**, 9005 (2021).

[51] W. J. Zhao, E. Runburg, Z. Y. Fei, J. Mutch, P. Malinowski, B. S. Sun, X. Huang, D. Pesin, Y. T. Cui, X. D. Xu *et al.*, Phys. Rev. X **11**, 041034 (2021).

[52] A. Arora, L. K. Shi, and J. C. W. Song, Phys. Rev. B **102**, 161402(R) (2020).